Skeletal Repair by in Situ Formation of the Mineral Phase of Bone

Brent R. Constantz,* Ira C. Ison, Mark T. Fulmer, Robert D. Poser, Susanne T. Smith, Michelle VanWagoner, John Ross, Steven A. Goldstein, Jesse B. Jupiter, Daniel I. Rosenthal

A process has been developed for the in situ formation of the mineral phase of bone. Inorganic calcium and phosphate sources are combined to form a paste that is surgically implanted by injection. Under physiological conditions, the material hardens in minutes concurrent with the formation of dahllite. After 12 hours, dahllite formation was nearly complete, and an ultimate compressive strength of 55 megapascals was achieved. The composition and crystal morphology of the dahllite formed are similar to those of bone. Animal studies provide evidence that the material is remodeled in vivo. A novel approach to skeletal repair is being tested in human trials for various applications; in one of the trials the new biomaterial is being percutaneously placed into acute fractures. After hardening, it serves as internal fixation to maintain proper alignment while healing occurs.

Bone is a composite material made up of organic and inorganic components. The mineral phase of bone comprises approximately 60 to 70% of the total dry bone weight while the remainder is comprised of organic materials (such as collagen) (*1*). Bone mineral is an apatitic calcium phosphate containing carbonate and small amounts of sodium, magnesium, and other trace components (*2*). This carbonated apatite, termed dahllite, contains 4 to 6% carbonate by weight (*3*) and is also the mineral constituent of teeth and of some invertebrate skeletons (*4*).

The most commonly used calcium phosphates for bone defect and trauma applications as implant coatings and defect fillers are thermally processed hydroxyapatite and tricalcium phosphate. Production of these materials involves processing at high temperatures, which results in preformed, highly crystalline, dense, bioinert ceramics. Such materials are very different from apatites that develop in vivo, and they have found limited application in orthopaedics because of their low fatigue properties relative to bone.

We report on a new process for the in situ formation of the mineral phase of bone. The process allows the surgical implantation of a paste that hardens in minutes under physiological conditions. Monocalcium phosphate, monohydrate [MCPM, $Ca(H_2PO_4)_2{\cdot}H_2O$], α-tricalcium phosphate [TCP, $Ca_3(PO_4)_2$], and calcium carbonate (CC, $CaCO_3$) are dry mixed. A sodium phosphate solution is added, and with subsequent mixing a paste is formed in a few minutes. The paste is formable and injectable for about 5 min and maintains physiologic temperature and pH. Upon delivery, the paste hardens due to crystallization of dahllite within about 10 min and attains an initial compressive strength of ~10 MPa. Within 12 hours, the material is about 85 to 90% dahllite and the final strength is achieved. The biomaterial attains a final maximum compressive strength of ~55 MPa and a tensile strength of ~2.1 MPa. Relative to cancellous bone, the compressive strength of the new biomaterial is greater while the tensile strength is about the same (*5*). By designing calcium phosphate implants of dahllite (carbonated apatite) which can be implanted as a surgical paste that hardens in situ, fractured bones can be held in place while the native bone remodeling process replaces the implant with living bone; thus an implant-bone composite is created. Replacement of dahllite implants by living bone may result in a progressively durable weight-bearing construct (*6*).

The bulk elemental constituents of the dahllite formed in this process under physiological conditions were determined by direct-current plasma spectrometry (*7*) and carbon coulometry (*8*). The calcium-to-phosphate molar ratio measured is ~1.67, and the carbonate content is ~4.6% by weight. From these measurements, we obtain the stoichiometric formula of the dahllite produced:

$$Ca_{8.8}(HPO_4)_{0.7}(PO_4)_{4.5}(CO_3)_{0.7}(OH)_{1.3}$$

Comparison of the Fourier transform infrared (FTIR) spectrum (*9*) of the mineral produced in the new process (Fig. 1) with that of stoichiometrically pure, sintered hydroxyapatite $[Ca_{10}(PO_4)_6(OH)_2]$ shows that this mineral is carbonated hydroxyapatite (dahllite), with some substitution by acidic phosphate (HPO_4^{2-}). Further, the absorption band at 871 cm^{-1} correlates to type B carbonated apatite as found in bone mineral in which the carbonate ions substitute for phosphate ions as opposed to hydroxyl ions (as in type A) (*10*).

Crystallographic analyses by powder x-ray diffraction (XRD) (*11*) were performed for the new dahllite material, sintered hydroxyapatite, and mammalian bone. The low count rates for both the dahllite material and mammalian bone as measured with standard XRD equipment necessitated the use of higher resolution equipment. Therefore, XRD analyses on both of these samples were performed at the Brookhaven National Light Source with high brilliance synchrotron x-rays (*12*) in order to attain the best possible signal-to-noise resolution available.

Synchrotron diffraction patterns for the new biomaterial and bone, as well as a standard XRD pattern of sintered hydroxyapatite are provided in Fig. 2. All of the patterns have peaks which correspond to apatite crystallographic structure, but the diffraction peaks are much more narrow and intense for the sintered material than for the bone or the new biomaterial. Diffraction peak intensity and width are greatly affected by crystallite size and lattice order (*13*). Larger, more highly ordered crystallites have many more uniformly spaced lattice planes available to contribute to diffraction count rate and peak sharpness than smaller crystallites (*13*). Thus, the sharp and intense peaks for the sintered material correspond to relatively large crystallites of high crystalline order. Conversely, the broadness and low intensities observed for the diffraction peaks of both bone and the

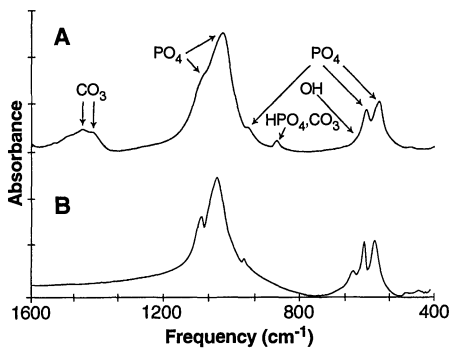

Fig. 1. FTIR spectra for (**A**) the new biomaterial and (**B**) sintered hydroxyapatite. The main peaks of sintered hydroxyapatite, although somewhat broadened, appear in the spectrum of the new biomaterial, in addition to new peaks due to carbonate and acid phosphate, which are also present in the mineral phase of bone.

B. R. Constantz, I. C. Ison, M. T. Fulmer, R. D. Poser, S. T. Smith, M. VanWagoner, Norian Corporation, Cupertino, CA 95014, USA.
J. Ross, Department of Chemistry, Stanford University, Stanford, CA 94305, USA.
S. A. Goldstein, Section of Orthopaedic Surgery, University of Michigan, Ann Arbor, MI 48109–0486, USA.
J. B. Jupiter and D. I. Rosenthal, Massachusetts General Hospital, Boston, MA 02114, USA.
*To whom correspondence should be addressed.

biomaterial are indicative of very small crystallite size and a large number of lattice defects most likely due to the carbonate incorporation detected by FTIR and carbon coulometry as an impurity in the apatite lattice. The remaining organic constituents within the bone sample may also contribute to the broadness and low intensity of peaks in that pattern.

Two methods were used to determine crystallite size. First, the Scherrer formula provides an estimate of the perfect crystallite size from peak widths and is

$$t = 0.9\lambda/(B\cos\theta)$$

where t is the crystallite size, λ is the wavelength of the x-rays, B is the full width at half maximum (FWHM), and θ is the angle of incidence upon the sample at the peak maximum (*13*). We used the 002 reflection to obtain average dimensions of perfect crystal domain of ~200 Å for both bone and the new biomaterial.

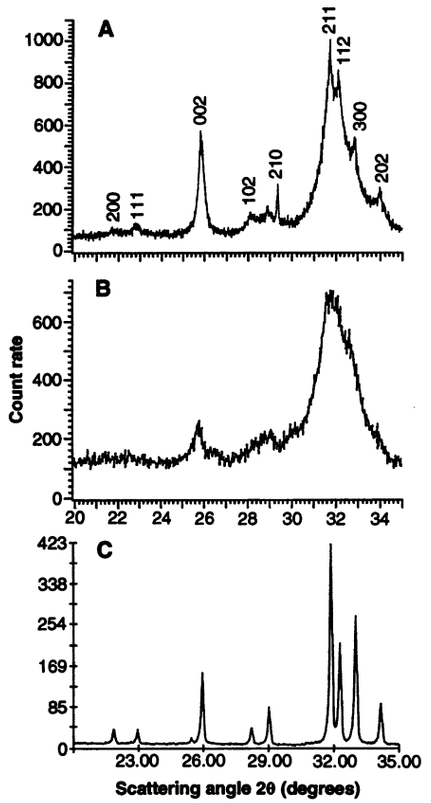

Fig. 2. Powder x-ray diffraction obtained at the Brookhaven National Synchrotron Light Source of (**A**) the new biomaterial and (**B**) rabbit cortical bone (count rate is 16K per second); (**C**) sintered hydroxyapatite XRD pattern was obtained with a Philips x-ray diffractometer (counts per minute). Miller indices (*13*) are labeled for the new biomaterial. The diffraction peaks of the new biomaterial are considerably broader than the sintered hydroxyapatite and resemble more closely the diffraction pattern of bone.

Application of the Reitveld refinement on the data from all of the XRD peaks simultaneously yields information regarding crystallite size, lattice defects, and impurities (*14*). Reitveld refinement confirms the average dimensions of crystallite size as determined by the Scherrer formula, and thus both techniques indicate that bone and the new biomaterial are similar with regard to average perfect crystallite size.

Transmission electron microscopy (TEM) (*15*) of the new biomaterial (Fig. 3) yields an estimate on the order of 500 Å for the average crystal size. Unlike bone, the single crystals comprising the new biomaterial have a nonpreferred, or random, orientation. This difference arises from the rapid formation of the new biomaterial in the absence of an organic matrix as compared to bone crystallites, which form slowly in a collagenous matrix (*16*).

The new biomaterial has a bulk density of 1.3 g/cm^3, as determined by mercury porosimetry (*17*). Gas porosimetry (*18*) indicates that the median average pore throat diameter is ~ 300 Å. These measurements and the TEM image indicate that the new biomaterial has nanophase porous structure.

The solubility of dahllite compared to stoichiometric hydroxyapatite is expected to be greater due to smaller crystallite size, increased lattice disorder, and impurities. In addition, both dahllite and hydroxyapatite become increasingly soluble with decreasing pH. Carbonated apatites, such as bone mineral, are substantially more soluble than sintered hydroxyapatite (*19*), and the same is predicted for the new biomaterial. The comparison of the solubility of the new biomaterial with that of bone is important because there is substantial evidence that osteoclasts resorb bone by producing an acidic microenvironment to dissolve bone mineral, which is otherwise nearly insoluble at neutral pH (*20*, *21*).

Replacement of the new biomaterial by living bone in animal studies appears to occur in a manner similar to bone remodeling (*22*). Figure 4 shows an undecalcified light histologic specimen (*23*) of the new biomaterial 2 weeks after implantation in the diaphysis of a rabbit's femur (*24*). Osteoclast and osteoblast cells are present at the interface of the new biomaterial, showing that the material is replaced by new living bone.

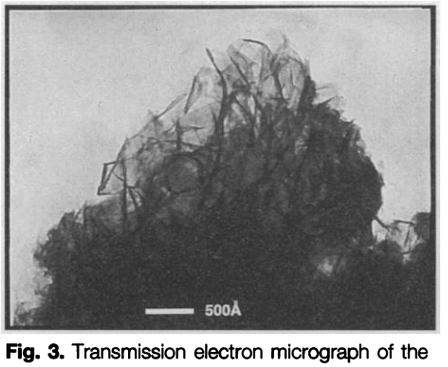

Fig. 3. Transmission electron micrograph of the new biomaterial after completion of dahllite formation. Magnification is ×100,000, and the scale bar represents 500 Å.

Figure 5 shows an electron micrograph of the new biomaterial implanted in a canine tibial metaphysis (*25*). Sixteen weeks after implantation (*26*), the extent of remodeling of the new biomaterial in the cortical bone region is essentially complete, whereas little remodeling has occurred in the region of cancellous bone (*6*, *27*).

Radiographic evidence from ongoing human studies (*28*) demonstrates that the material can be implanted percutaneously into an acute fracture and can be incorporated within the fracture defect to provide internal fracture stabilization during the healing process. Figure 6 shows x-rays (*29*)

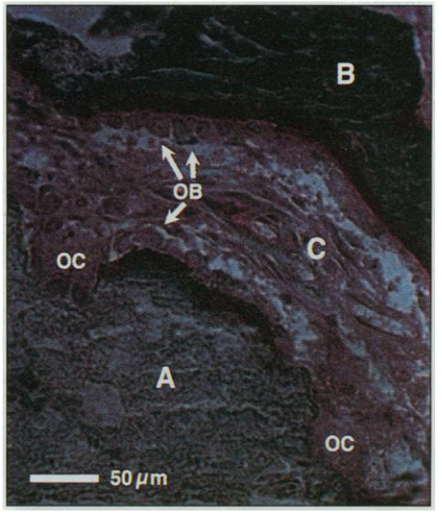

Fig. 4. A polarized light micrograph of a rabbit diaphysis implanted with the new biomaterial after 2 weeks: (**A**) the new biomaterial; (**B**) the native bone; and (**C**) a Haversion canal in which osteoclasts (OC) and osteoblasts (OB) are observed remodeling the biomaterial. The scale bar represents 50 μm.

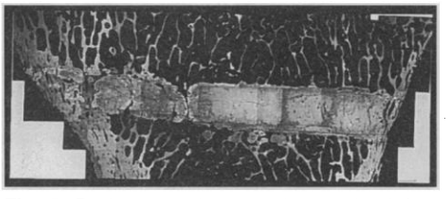

Fig. 5. Backscatter electron micrograph of the new biomaterial in a canine metaphyseal defect at 16 weeks post-implantation. Reestablishment of host tissue occurs at a much greater rate in the region of cortical bone and carries relatively greater amounts of load as compared to the cancellous regions.

Table 1. Results from wrist fracture patients treated by percutaneous injection of the new biomaterial into acute fractures of the distal radius. The new biomaterial was allowed to harden in situ for 15 min before the patient's arm was casted. Casts were removed 6 weeks later. Radiographic measurements (for example, radial length), functional measurements (such as grip strength), and incidence of failure (loss of reduction) will be monitored for up to 1 year. The improved maintenance of radial length (*30*) compared to the historical controls (*31*), which use conventional casting, suggests that the new biomaterial's presence in the fracture site resisted the compressive forces from the musculature across the wrist fracture and allowed the displaced bone fragments to heal while held in the normal anatomical position. In the historical control cases, the bone fragments settled under the compressive forces, and the radius healed shorter than the normal anatomical position. In comparison, the hand function for patients treated with the new biomaterial was improved and achieved rapidly. By 6 months, the patients treated with the new biomaterial had surpassed the grip strengths (*32*) of the historical controls, even at 2 years. None of the patients treated with the new biomaterial failed reduction, which requires re-reduction and another procedure. With conventional techniques, these fractures typically lose reduction and require re-reduction in at least 20% of the cases (*33*).

Clinical outcome	Time after injection			Historical control
	6 weeks	3 months	6 months	
Loss of radial length (mm)	1.4	1.6	1.6	4.6*
Grip strength (%)	n/a	66	83	78†
Failure rate (%)	0	0	0	20‡

*Thirteen-week average follow-up. †Two-year average follow-up. ‡One-year average follow-up (*31*).

of the wrist of a 49-year-old female who fractured the distal radius as the result of a fall. The fracture was clinically unstable because of comminution of the dorsal cortex. Implantation of the new biomaterial permitted stabilization of fractured bone and maintenance of correct position.

The new biomaterial offers useful rheological and structural characteristics together with the potential for replacement with natural bone by cell mediated healing. Also, it can be implanted by the minimally invasive means of injection. These properties make it ideal for applications involving skeletal defects under predominantly compressive loads, such as the filling of voids or bony defects, the restoration of normal bone geometry, the augmentation of implant attachment to bone, and the filling of bone gaps associated with internal fixation. This material may be particularly suited to the repair of mechanically compromised osteoporotic bone. It has been used in human trials in different applications, including wrist fractures (Colles' fractures), tibial plateau fractures, spinal reconstruction, humeral head fractures, acetabular cup revision, and frontal sinus lifts. Clinical investigations in wrist fractures suggest improved anatomical outcome, hand function, and rate of success for patients treated with the new biomaterial when compared to current standard methods of fracture fixation (Table 1).

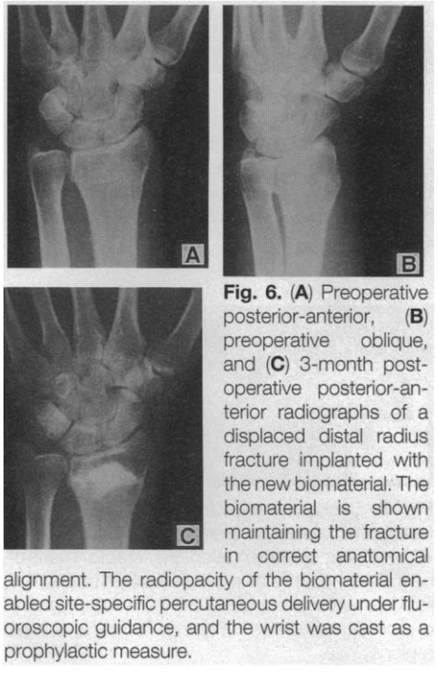

Fig. 6. (**A**) Preoperative posterior-anterior, (**B**) preoperative oblique, and (**C**) 3-month postoperative posterior-anterior radiographs of a displaced distal radius fracture implanted with the new biomaterial. The biomaterial is shown maintaining the fracture in correct anatomical alignment. The radiopacity of the biomaterial enabled site-specific percutaneous delivery under fluoroscopic guidance, and the wrist was cast as a prophylactic measure.

REFERENCES AND NOTES

1. A. S. Posner, N. C. Blumenthal, F. Betts, *Phosphate Minerals*, L. O. Nriagu and P. B. Moore, Eds. (Springer-Verlag, New York, 1984), pp. 330–350.
2. M. J. Glimcher, L. C. Bonar, M. D. Grynpas, W. J. Landis, A. H. Roufosse, *J. Cryst. Growth* **53**, 100 (1981).
3. D. McConnell, *J. Dent. Res.* **31**, 53 (1952).
4. H. A. Lowenstam and S. Weiner, *On Biomineralization* (Oxford Univ. Press, Oxford, 1989), pp. 144–162.
5. L. Rohl, E. Larsen, F. Linde, A. Odgaard, and J. Jorgensen [*J. Biomech.*, **24**, 1143 (1991)] report the ultimate compression strength of cancellous bone to be 1.9 ± 0.14 MPa and the ultimate tensile strength to be 2.42 ± 0.16 MPa.
6. E. P. Frankenburg *et al.*, *Transactions of the 40th Annual Meeting* (Orthopaedic Research Society, Rosemont, IL, 1994), vol. 19, section 1, pp. 157–227.
7. Elemental analyses were performed with a Spectraspan III DC plasma spectrometer on samples microwave digested in concentrated HCl. Standards were prepared by diluting 1000 parts per million stock solutions to suitable concentrations.
8. Total inorganic carbonate analyses were performed on the biomaterial with a Coulometrics Carbon Coulometer equipped with an acidification unit for CO_2 removal.
9. Biomaterial samples were ground with a mortar and pestle. FTIR spectroscopy was performed on 1-mg samples pressed in KBr pellets with a Nicolet 5DXC FTIR Spectrometer.
10. C. Rey, V. Renugopalakrishnan, B. Collins, M. J. Glimcher, *Calcif. Tissue Int.* **49**, 251 (October 1991).
11. Powder x-ray diffraction measurements (Cu Kα radiation) were performed on biomaterial samples ground with a mortar and pestle, packed in aluminum sample holders, and scanned with a Philips XRG 5000 fitted with a 42271/0 goniometer.
12. Synchrotron powder diffraction was performed at the National Synchrotron Light Source at Brookhaven National Laboratory. Biomaterial samples were ground with a mortar and pestle and analyzed on beamline X10A configured with a focusing mirror and two-crystal monochromator with a pair of Ge(111) crystals.
13. B. D. Cullity, *Elements of X-Ray Diffraction* (Addison-Wesley, Reading, MA, ed. 2, 1978), pp. 99–106.
14. J. E. Post and D. L. Bish, Eds., *Modern Powder Diffraction*, vol. 20 of *Reviews in Mineralogy* (Mineralogical Society of America, Washington, DC, 1989), pp. 277–308.
15. The biomaterial was ground with a mortar and pestle and aerosol-dispersed onto TEM grids with carbon substrate. After carbon coating, all of the samples were examined with a JEOL-1200 EX TEM at 100 kV at a magnification of 100,000×.
16. L. Addadi and S. Weiner, *Proc. Natl. Acad. Sci. U.S.A.* **82**, 4110 (1985).
17. Bulk density was determined with a Micromeritics Autopore II 9220 mercury porosimeter with an evacuation pressure of 50 mm of mercury and a mercury filling pressure of 1.55 pounds per square inch absolute.
18. Average pore size was determined with a Micromeritics ASAP 2400 gas porosimeter.
19. D. G. A. Nelson, *J. Dent. Res.* **60**, 1621 (1981).
20. G. Vaes, *Clin. Orthop. Relat. Res.* **231**, 239 (1988).
21. H. C. Blair, S. L. Teidelbaum, H. L. Tan, C. M. Koziol, P. H. Schlesinger, *Am. J. Phys.* **260**, C1315 (1991).
22. B. R. Constantz *et al.*, *Mater. Res. Soc. Symp. Proc.* **252**, 79 (1992).
23. A portion of tissue implanted with the new biomaterial was processed histologically for hard tissue. It was embedded in resin and thin sectioned with an ultramicrotome fitted with a diamond blade. The specimen was mounted on a slide and trichrome stained. Optical microscopy was performed with polarized light.
24. Animal care was conducted under the Animal Care Committee guidelines of the Letterman Army Institute of Research. The following anesthetic agents were used in this experiment: ketamine HCl [20 mg/kg intravenous (iv)] and xylazine HCl (7 mg/kg iv).
25. The specimen was polished to attain a mirrorlike finish for optimal signal collection. Backscatter images were obtained by using Rutherford backscatter utilizing a Hitachi S-570 SEM at 25 kV and 15 mm working distance. The original magnification was 25×. Images were used to produce a montage and then subsequently reduced.
26. Animal care was conducted under the Animal Care Committee guidelines of the University of Michigan, Orthopaedic Research Laboratory. The following anesthetic agents were used in this experiment: atropine (0.04 mg/kg intramuscular), 5% suritol (1 cubic centimeters per 5 pounds body weight iv to effect), and halothane/O_2 (inhalant).
27. This observation suggests that remodeling of the biomaterial occurs more readily in regions through which greater amounts of load are transferred (that is, cortical bone) and to a much lesser extent in those regions through which relatively less load is transferred (that is, regions of cancellous bone), akin to the principles of normal bone remodeling [J. Wolff, *Das Gesetz der Transformation der Knochen* (Hirshwald, Berlin, 1892)].
28. Human clinical experiments were performed in compliance with the U.S. Food and Drug Administration Investigational Device Exemption, which requires a subject's informed consent prior to study participation.
29. A standardized radiographic technique was used to minimize variation of limb position and radiographic measurements longitudinally.

30. J. B. Jupiter, *J. Bone J. Surg. Am. Vol.* **73**, 461 (1991).
31. J. J. Dias, C. C. Wray, J. M. Jones, *Injury* **18**, 304 (1987); C. Pool, *J. Bone Jt. Surg. Br. Vol.* **55**, 540 (1973); A. Schmalholz, *Clin. Orthop. Relat. Res.* **254**, 236 (1990).
32. E. Fess, *Clinical Assessment Recommendations* (American Society of Hand Therapists, Chicago, 1992), pp. 41–45.
33. In a pilot wrist fracture clinical study conducted at Lund University Hospital, Lund, Sweden, which treated patients who had already failed reduction under conventional casting, patients had their fractures re-reduced and the new biomaterial was introduced. The patients were then re-casted; the cast was left on for only 2 weeks, then removed, and the patients were allowed to begin physical therapy. These patients achieved functional recovery very early, suggesting that extended casting (6 weeks) or immobilization through external fixation (8 to 10 weeks) could be shortened significantly or eliminated completely when the new biomaterial has been implanted in the fracture site.
34. We thank the reviewers for useful comments and the assistance of the Brookhaven National Laboratory (K. D'Amico), the Letterman Army Institute of Research (J. Baker, W. Rodkey, T. Bozo, D. Fredericks, W. Bergman, and L. McKinney), the University of Michigan Orthopaedic Research Laboratory and the Cleveland Clinic Foundation (E. Frankenburg, T. Bauer, J. Baker, and K. Sweet), Massachusetts General Hospital (L. Goodman, S. Simpson, S. Winters, S. Sigmund, C. Pappas, and C. Lowe), and Norian Corporation (R. Sakai, who prepared all aspects of the manuscript, K. Alcorn, and B. Barr) whose participation made this report possible.

7 September 1994; accepted 18 January 1995

Spontaneous Magnetic Ordering in the Fullerene Charge-Transfer Salt (TDAE)C_{60}

A. Lappas, K. Prassides,* K. Vavekis, D. Arcon, R. Blinc, P. Cevc, A. Amato, R. Feyerherm, F. N. Gygax, A. Schenck

The zero-field muon spin relaxation technique has been used in the direct observation of spontaneous magnetic order below a Curie temperature (T_C) of ~16.1 kelvin in the fullerene charge-transfer salt (tetrakisdimethylaminoethylene)C_{60} [(TDAE)C_{60}]. Coherent ordering of the electronic magnetic moments leads to a local field of 68(1) gauss at the muon site at 3.2 kelvin (parentheses indicate the error in the last digit). Substantial spatially inhomogeneous effects are manifested in the distribution of the local fields, whose width amounts to 48(2) gauss at the same temperature. The temperature evolution of the internal magnetic field below the freezing temperature mirrors that of the saturation magnetization, closely following the behavior expected for collective spin wave (magnon) excitations. The transition to a ferromagnetic state with a T_C higher than that of any other organic material is now authenticated.

Intercalation of solid C_{60} with electron donors, such as the alkali metals, can lead to metallic compositions of stoichiometry A_3C_{60} that become superconducting (*1*) at critical temperatures as high as 33 K, surpassed only by the superconducting cuprates with high superconducting transition temperatures. Reactions of C_{60} with strong organic donors, such as tetrakisdimethylaminoethylene, $C_2N_4(CH_3)_8$ (Fig. 1), also result in materials with interesting properties. The charge-transfer salt with stoichiometry (TDAE)C_{60} develops a large magnetic susceptibility below ~16.1 K, consistent with a transition to a ferromagnetic state (*2*). The lack of any observed remanent magnetization or hysteresis was interpreted in terms of "soft" ferromagnetism (*3*) in a highly anisotropic solid, as necessitated by a crystal structure in which there were relatively short (~9.96 Å) intermolecular contacts along the *c* axis (*4*). The ferromagnetic state was also found to be highly sensitive to applied pressure, with both the magnetic moment and the transition temperature decreasing rapidly (*3*, *5*). The conductivity at room temperature is of the order of $\sim 10^{-4}$ ohm^{-1} cm^{-1} and shows a nonmetallic temperature dependence (*6*). Despite numerous efforts with various experimental techniques, such as magnetization (*7*), electron spin resonance (ESR) (*7–10*), and nuclear magnetic resonance (NMR) (*9*, *11*) measurements, the origin and true nature of the low-temperature magnetic phase has remained the subject of controversy, encompassing the possibilities of field-induced "weak" ferromagnetism, "itinerant" ferromagnetism, "spin glass"–like ordering, and "superparamagnetic"-type ordering. However, as yet the most fundamental parameter of a ferromagnet, the spontaneous magnetization in zero applied field, has remained uninvestigated.

Here, we address the problem of the existence of nonzero internal local fields in the low-temperature phase of (TDAE)C_{60}. We investigated this problem by using 100% spin-polarized positive muons (μ^+) in the absence of external fields. These muons are implanted into the solid sample and, after they come to rest at an interstitial site, they act as highly sensitive microscopic local magnetic probes. In the presence of local magnetic fields ($\langle B_\mu \rangle$), they will precess with a frequency given by

$$\nu_\mu = (\gamma_\mu/2\pi)\langle B_\mu \rangle \quad (1)$$

where $\gamma_\mu/2\pi = 13.55$ kHz G^{-1}. In the absence of an applied external field, the appearance of precession signals the onset of an ordering (ferromagnetic or antiferromagnetic) transition. Moreover, application of a magnetic field parallel to the initial muon spin polarization [longitudinal field (LF)] allows the decoupling of the μ^+ spin from the static internal fields. Muon spin relaxation (μ^+SR) spectroscopy has proven extremely powerful in cases of small-moment magnetism and in all instances where magnetic order is of a random, very short range, spatially inhomogeneous or incommensurate nature (*12*). In (TDAE)C_{60}, we observed a heavily damped oscillating signal, which provides unambiguous proof of the existence of long-range magnetic order below ~16.1 K. The strong relaxation found in zero field (ZF) is the signature of spatial disorder and inhomogeneity effects. In addition, we found that the precession frequency varies with temperature on approaching the Curie temperature (T_C) in a different manner from that expected on the basis of the mean-field treatment of a three-dimensional Heisenberg exchange model. It appears that magnon excitations dominate the magnetic behavior, even at temperatures close to T_C, thus providing an explanation of the observed properties, such as the "soft" magnetic behavior, the small saturated moment per molecule [0.33 Bohr magneton (μ_B) at 5 K], the pressure sensitivity of the magnetic properties, and the spatial disorder.

We collected ZF and LF (10 to 1000 G) μ^+SR data on (TDAE)C_{60} (*13*) at the Paul Scherrer Institute (PSI), Villigen, Switzerland, with the general purpose spectrometer, using low-energy (surface) muons on the μ^+SR-dedicated πM3 beamline on the PSI 600-MeV proton accelerator. The 120-mg powder sample was sealed under Ar in an Ag sample holder equipped with In seals

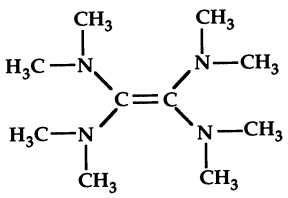

Fig. 1. The TDAE molecule.

A. Lappas, K. Prassides, K. Vavekis, School of Chemistry and Molecular Sciences, University of Sussex, Brighton BN1 9QJ, U.K.
D. Arcon, R. Blinc, P. Cevc, J. Stefan Institute, University of Ljubljana, 61111 Ljubljana, Slovenia.
A. Amato, R. Feyerherm, F. N. Gygax, A. Schenck, Institute for Particle Physics, Swiss Federal Institute of Technology (ETH) Zürich, CH-5232, Paul Scherrer Institute, Villigen, Switzerland.
*To whom correspondence should be addressed.